



HAL
open science

Stereoactive Electron Lone Pairs Facilitate Fluoride Ion Diffusion in Tetragonal BaSnF₄

Xiliang Lian, Damien Dambournet, Mathieu Salanne

► **To cite this version:**

Xiliang Lian, Damien Dambournet, Mathieu Salanne. Stereoactive Electron Lone Pairs Facilitate Fluoride Ion Diffusion in Tetragonal BaSnF₄. *Chemistry of Materials*, 2024, 10.1021/acs.chemmater.4c02756 . hal-04842002

HAL Id: hal-04842002

<https://hal.sorbonne-universite.fr/hal-04842002v1>

Submitted on 17 Dec 2024

HAL is a multi-disciplinary open access archive for the deposit and dissemination of scientific research documents, whether they are published or not. The documents may come from teaching and research institutions in France or abroad, or from public or private research centers.

L'archive ouverte pluridisciplinaire **HAL**, est destinée au dépôt et à la diffusion de documents scientifiques de niveau recherche, publiés ou non, émanant des établissements d'enseignement et de recherche français ou étrangers, des laboratoires publics ou privés.



Distributed under a Creative Commons Attribution 4.0 International License

Stereoactive Electron Lone Pairs Facilitate Fluoride Ion Diffusion in Tetragonal-BaSnF₄

Xiliang Lian,^{†,‡} Damien Dambournet,^{†,‡} and Mathieu Salanne^{*,†,‡,¶}

[†]*Sorbonne Université, CNRS, Physicochimie des Électrolytes et Nanosystèmes Interfaciaux, F-75005 Paris, France*

[‡]*Réseau sur le Stockage Electrochimique de l'Energie (RS2E), FR CNRS 3459, 80039 Amiens Cedex, France*

[¶]*Institut Universitaire de France (IUF), 75231 Paris, France*

E-mail: mathieu.salanne@sorbonne-universite.fr

Abstract

Solid state ionic conductors are of primary importance for the design of tomorrow's batteries. In lithium ion or sodium ion-based materials, the alkali cations diffuse through three-dimensional channels consisting of interconnected tetrahedral or octahedral sites with low free energy barriers between them. Fluoride ion conductors stand out in this landscape since the materials with the highest conductivities belong to the MSnF₄ family (in which M²⁺ is a divalent cation), which structure is layered and characterized by double-layers of Sn²⁺ and M²⁺ cations along a given direction. Importantly, these materials display stereoactive electron lone pairs (LPs) that seemingly play an important role not only in stabilizing of the Sn-Sn layer but also in modulating the fluoride ion diffusive behavior. However, despite previous experimental and simulation studies, the involvement of the LPs in the fluoride ions conduction mechanism remains to be quantitatively understood. In this work, we simulate the BaSnF₄ tetragonal structure using machine learning-based molecular dynamics, in which the interaction potential

is trained on density functional theory data. We investigate the role of the Sn-LP-Sn layer in lowering the diffusion energy landscape. In particular, we show how the F^- ions jump across this layer occur much more frequently than in the Ba-F-Ba one, resulting in the formation of vacancies in the Ba-Sn layers. Concurrently, the LPs stereochemical activity fluctuates to accommodate the F ions jumping. In addition, the presence of the LP layer enhances the flexibility of the Sn ions, which leads to an increase of the two-dimensional diffusion by several orders of magnitude. These results contribute to the understanding of the interplay between LPs and ionic diffusion, helping to explain the good performance of the material in fluoride-ion batteries.

Introduction

The Li-ion battery is increasingly being used in modern society, in applications ranging from electronic devices and electric vehicles to grid storage. However, the needs for the latter application are very large, and they may not be met due to the limited availability of lithium and of other critical transition metal (i.e. Ni, Co) resources. Intensive research efforts have thus been placed on “post-lithium” batteries in recent years. Fluoride ion battery (FIB) is a potential alternative due to the fluorine earth abundance, high theoretical volumetric energy density and potentially wide electrochemical stability window.^{1,2} Since the initial proof of concept of a rechargeable FIB,³ its development has however been plagued by the low room-temperature fluoride ionic conductivity in solid electrolytes. Among the various studied materials, $BaSnF_4$ is a promising candidate with a suitable ionic conductivity of $3.5 \times 10^{-4} \text{ S cm}^{-1}$ at ambient temperature.^{2,4} It has indeed been successfully used in FIBs,⁵⁻⁷ and some efforts are currently devoted to increase further the fluoride ion diffusivity by composition tuning.^{8,9} However, the conduction mechanism and the main structural factors that control the fluoride ion mobility in $BaSnF_4$ have not been elucidated yet.

Tetragonal $BaSnF_4$ displays a fluorite structure made of alternating [-Ba-Ba-Sn-Sn-] layers as shown in Figure 1. The fluoride ions reside between Ba-Ba (F_{2b}) and Ba-Sn layers

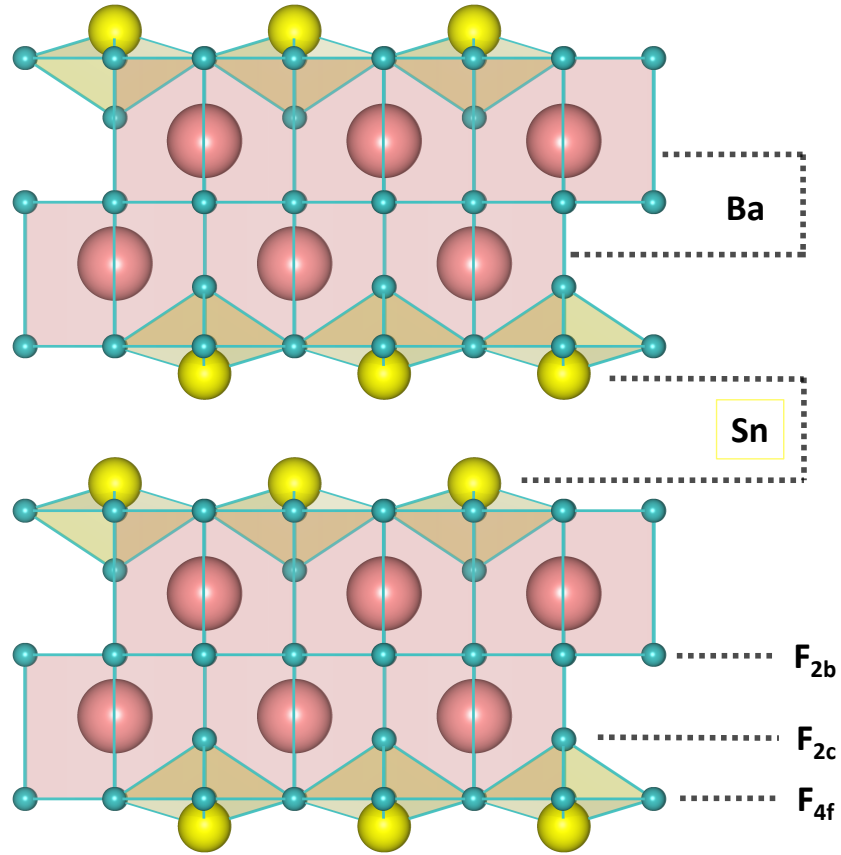


Figure 1: Layered structure of BaSnF₄. Ba, Sn and F atoms are displayed as pink, yellow, and cyan spheres. The cubic and square pyramid coordination for Ba and Sn atoms are shown in light pink and light yellow shades. The cyan solid lines denote the Ba-F and Sn-F bonds. The subscription for F label corresponds to the Wyckoff positions of different F sites. The F atoms between Ba-Ba layer are labeled as 2b and those between the Ba-Sn layers are labeled as 2c and 4f.

(F_{2c} and F_{4f}).^{10,11} Earlier NMR work concluded that F^- ions between Ba-Ba layers are almost immobile while those between Ba-Sn layers undergo rapid exchanges.⁴ Similar behavior has been observed in the isomeric cubic phase $BaSnF_4$ (termed as *c*- $BaSnF_4$), where the cations Sn^{2+} and Ba^{2+} display composition disorder, identified as Sn-rich and Ba-rich regions. The former features enhanced fluoride ion dynamics compared to Ba-rich ones.¹² Tetragonal $BaSnF_4$ is characterized by the existence of stereoactive electron LPs located on the Sn atoms, which leads to a depletion of the F^- ions in the Sn-LP-Sn layer, resulting in an empty gap. The LP stereoactivity was noticed since the initial work,¹⁰ then confirmed using Mössbauer spectroscopy with a characteristic quadrupole splitting and later characterized by ^{119}Sn MAS NMR spectra with a large spinning sideband.^{10,11,13} However, the previous studies on tetragonal $BaSnF_4$ could not shed light on the role of the LPs in the fluoride ion diffusion mechanisms. In other systems, LPs were shown to drastically impact the physical properties; for example they lead to ultralow thermal conductivity in aikinite,¹⁴ favor a phase transition in $SnMoO_4$,¹⁵ as well as energy flattening in $CsPb_{0.9}K_{0.1}F_{2.9}$ ¹⁶ and other exotic properties.¹⁷

The ionic conductivities trend in $PbSnF_4$, $BaSnF_4$, and $BaMgF_4$ manifests evident correlations with the presence of LPs, with $\sigma_{PbSnF_4} > \sigma_{BaSnF_4} \gg \sigma_{BaMgF_4}$.^{2,5,18} The $PbSnF_4$ is isostructural to $BaSnF_4$, with a slightly higher ionic conductivity (1×10^{-3} S cm^{-1} at ambient temperature). Moreover, Pb^{2+} , with an electronic configuration of $[Xe]4f^{14}5d^{10}6s^2$, also possesses stereoactive LPs ($6s^2$) albeit these display a lesser tendency to stereoactivity.¹⁹ At elevated temperature, $PbSnF_4$ shows almost isotropic rapid diffusion behavior²⁰ while the fluoride ions in $BaSnF_4$ predominately move along the XY plane according to NMR spectroscopy results.²¹ Contrarily, in the absence of LPs, $BaMgF_4$ structure deviates from $BaSnF_4$ and shows a very small ambient temperature ionic conductivity of 1×10^{-8} S cm^{-1} , four orders of magnitude lower than $BaSnF_4$.¹⁸ Therefore, it seems that LPs significantly improve the fluoride ion mobilities in fluoride ion conductors, and it would be of great benefit to understand the atomistic origin of this enhancement.

Interestingly, the role of the LPs has been studied in other ionic conductors recently. For example, the F^- ions migration barrier of KF-doped $CsPbF_3$ were found to be four times smaller than that of isostructural $CsSrF_3$, highlighting the important role of LPs. They were shown to stabilize the saddle-point structure when F^- ions exchange with neighboring vacancy, thereby lowering the barrier energy.¹⁶ In $c\text{-BaSnF}_4$, the Sn dipole autocorrelation function (ACF) of the freely mobile F^- ions decay to a non-zero value on a picosecond timescale, showing preferential orientation of the LPs. When restricting the F^- ions motion, ACF quickly decays to 0, indicating the coupling between LP dynamics and local F^- motion. This coupling originates from LPs' tendency to reorient towards the Sn clusters, thereby disrupting the tetrahedral site occupations, promoting the dynamics in the Sn-rich region.¹² LPs were also shown to play a significant role in the AgI ionic conductor. An electronic "paddle-wheel" mechanism was evidenced, in which the iodine lone pairs rotation is accompanied by Ag^+ diffusion from site to site.²²

However, these mechanisms may not take place in $BaSnF_4$, in which the LPs are expected to be more stereochemically active than that in $CsPbF_3$ and much more ordered than in $c\text{-BaSnF}_4$. Indeed, the layered structure $BaSnF_4$, with LPs located within the Sn-LP-Sn layers strongly suggests other factors modulate the fluoride ion dynamics. In this article, we use machine learning-based molecular dynamics (ML-MD) to investigate the interplay between structure and dynamics in $BaSnF_4$. In particular, the use of ML-MD allows us to simulate long trajectories and gather many diffusive events, which is necessary for computing accurately the free energy changes associated to each migration mechanism. Our results show that the LPs behave very differently from the case of other materials. In particular, no exchange with the fluoride ions is observed, contrarily to the case of KF-doped $CsPbF_3$. Instead, the layering of the LPs allows frequent and rapid jumps of fluoride ions from one Ba-F-Sn layer to another, leading to the formation of vacancies in the original Ba-F-Sn layer. The lone pairs slightly contract when the F^- ion resides in the Sn-LPs-Sn layer, leading to the formation of the transition state. Furthermore, the LPs flexibility is evidenced by the

importance of Sn translational motion, which modifies the structural parameters to facilitate the ionic diffusion. As a consequence, the two-dimensional diffusion coefficients of the ions within these layers are enhanced by several orders of magnitude. Finally, we piece together all the information and provide a complete picture of fluoride ion conduction process in BaSnF₄.

Methods

Density functional theory-based molecular dynamics reference calculations

All the electronic structure calculations were performed using the Vienna Ab initio Simulation Package (VASP)^{23,24} within the density functional theory (DFT) framework. The exchange-correlation energy is approximated using the revised Perdew-Burke-Ernzerhof (PBE) generalized gradient approximation PBEsol exchange-correlation functional and the core-valence interactions are described by the projector-augmented wave (PAW) method as implemented in VASP. The valence configurations for Ba, Sn and F are $5s^25p^66s^2$, $4d^{10}5s^25p^2$, and $2s^22p^5$ respectively. The initial structure was obtained from experiments and structural relaxation was performed with a kinetic energy cutoff of 600 eV and K spacing of 0.25 Å⁻¹. The energy convergence threshold was set to 10⁻⁶ eV and the forces were converged to 0.01 eV Å⁻¹. The optimized structure is used to construct a 3×3×1 supercell for density functional theory-based molecular dynamics (DFT-MD) simulations.

We then performed DFT-MD simulations at 600 and 900 K for comparison with ML-MD as discussed in the following section. Gamma point was used to sample Brillouin zone to increase efficiency and the kinetic energy cutoff was set to 500 eV. The Newton's equation of motion is integrated using Verlet algorithm with a timestep of 1 fs. The canonical ensemble, where the number of particles, the volume and the temperature are fixed (NVT), was used for the simulation. The temperature is controlled by Nose-Hoover chains thermostat.

Machine learning-based molecular dynamics

An on-the-fly machine learning potential as implemented in VASP was trained based on the DFT-MD simulation performed on the $3\times 3\times 1$ supercell from 500 K to 1000 K at a heating rate of 2 K ps^{-1} . The initial configuration was equilibrated for 50 ps using the on-the-fly training. Then, the potential was abandoned and the equilibrated structure served as starting structure for the machine learning potential training. A brief introduction to the theory has been given in our previous work²⁵ and more detailed formulations can be found from Ref. 26–28. As shown in our previous work, the model can yield excellent agreements with results from DFT-MD at room temperature. The cutoff radius for radial and angular descriptors were set to 8 Å and 5 Å respectively. All other hyperparameters were set to the same values as in our previous work.²⁵

To ensure the accuracy of the machine learning potential in our working temperature range, we performed simulations at 600 K and 900 K. First, at each temperature, 100 configurations were selected from DFT-MD trajectory, based on which the forces were computed using the machine learning potential and DFT. The forces differences in Supplementary Figures S1 and S3 exhibit random distribution with a root mean square error (RMSE) for forces differences at 900 K of 64 meV Å⁻¹. Furthermore, we compared the radial distribution function (RDF) at respective temperatures and obtained excellent agreement between DFT-MD and ML-MD as illustrated by Supplementary Figures S2 and S4. More specifically, we notice that at 600 K, the Sn-Sn RDF first peak displays a splitting at around 4 Å which disappears at 900 K. The peak splitting and merge have been accurately captured by our model.

To compute mean square displacements (MSD) and ionic conductivities, we build a larger $5\times 5\times 2$ supercell from the unit cell. Then, all the starting configurations for ML-MD were obtained by gradually heating the initial configurations from 100 K to target temperatures. We estimated the error bar by performing three independent calculations at each temperature with a minimum simulation time of 10 ns.

To investigate the role of Sn translational motion, we setup two additional calculations

with Sn atoms being mobile and fixed using a $3 \times 3 \times 1$ supercell. The calculations settings were the same as previously except for the simulation time, which was extended to 20 ns. Except for computing the ionic conductivities, all the analysis were done with simulations at 900 K using a $3 \times 3 \times 1$ supercell unless specified in the text. To determine the orientations of the LPs, we computed the maximally localized Wannier functions using the Wannier90 code.²⁹ This was done by sampling the initial 10 ps trajectory at 100 fs intervals, resulting in 100 structures. Then, the Sn ions individual dipoles (μ_i) are given by:³⁰

$$\mu_i = -2 \sum_{j, |\mathbf{r}_j - \mathbf{R}_i| < R_{\text{cut}}} (\mathbf{r}_j - \mathbf{R}_i) \quad (1)$$

where \mathbf{R}_i is the position of atom i , \mathbf{r}_j the position of the center of the j th Wannier function and R_{cut} a cut-off distance to attribute the functions to a specific atom (here we took $R_{\text{cut}} = 1.5 \text{ \AA}$). The -2 prefactor arises from the presence of 2 electrons in each Wannier function. In the interpretation, we assume that the Sn dipole direction provides the LP position as in our previous work.²⁵ All the analysis in this work were realized using VASPKIT,³¹ pymatgen,³² and MDAnalysis.^{33,34}

X-ray total scattering

High energy X-ray data were collected at the 11-ID-B station at the Advanced Photon Source (Argonne National Laboratory) by our experimental partners. After corrections (background and Compton scattering), the pair distribution function (PDF) was extracted from the data using PDFgetX2 software.³⁵ Refinements of the PDF data were performed using PDFgui.³⁶ For the tetragonal model, the refined parameters include lattice parameters, atomic fraction coordinates, scale factor, s ratio (i.e., low- r to high- r PDF peak ratio correction because of the correlated motion of bonded atoms), and isotropic atomic displacement factors (ADPs). For the computed model, the atomic fraction coordinates were left unrefined.

The quality of the refinements was quantified by the reliability factor weighted R -value,

denoted as R_w . The R -value describes the difference between the experimental observation (data) and the calculated value (fit) for a single data point. The R_w is the R -value weighted for data point i , and is given by the formula:

$$R_w = \sqrt{\frac{\sum_{i=1}^N w(r_i)[G_{obs}(r_i) - G_{calc}(r_i)]^2}{\sum_{i=1}^N w(r_i)G_{obs}(r_i)^2}} \quad (2)$$

with G_{obs} and G_{calc} being the observed (data) and calculated (fit) PDF and $w(ri)$ being the weight for each data point.

Results and Discussions

Structural characterization

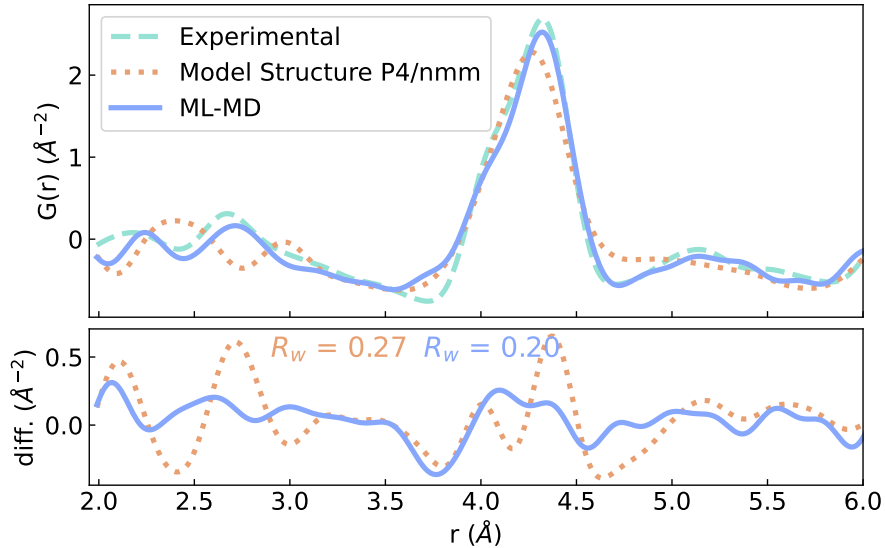


Figure 2: Real-space refinements of the PDF data using the experimental (cyan, dashed), model structure with space group P4/nmm (orange, dotted), and the ML-MD-equilibrated structure at 300 K (blue, solid). Lower panel: differences of the two models with respect to the experimental model. The R_w is defined in the main text.

Before examining the diffusion properties occurring in BaSnF_4 , we first confront the computed structure to the measured x-ray PDF data. We considered two set of models that

we analyzed by real-space refinement. The first tested model was that of Ahmad *et al.*,¹¹ who solved and described the structure by Rietveld analysis of powder x-ray diffraction data. The refinement (see methods for details) was performed within the inter-atomic distances that reflects the local structure, i.e. from 2 to 6 Å. The real-space refinement obtained using the crystal structure is shown in Figure 2 upper panel. It shows that the model fails to reproduce some of the inter-atomic distances, particularly those located at around 4 Å, assigned to Sn-Sn distances. This emphasizes that the local structure deviates from the average one, most particularly for the Sn sublattice. Subsequently, we used a computed model obtained by equilibrating the relaxed structure for 20 ns at 300 K using ML-MD. To limit the number of refined parameters, the fractional atomic coordinates were constrained to those obtained by the simulation. Using this computed model led to an appreciable improvement of the fit (despite the limited number of refined parameters) with a reliability factor decreasing from 27 to 20%, as shown in Figure 2 lower panel. Such improvement is assigned to a better reproducibility of the Sn-Sn distances, highlighting a distortion of the Sn-Sn arrangement. This shows the accuracy of the ML-MD simulation to describe the structural features of BaSnF₄ and motivated us to dig further on the Sn sublattice dynamics.

Stereoactivity of the lone pairs

In order to illustrate the stereoactivity of the Sn atoms electron lone pairs, we have calculated the electron localization function (ELF) for the optimized geometry of tetragonal BaSnF₄;³⁷ it is shown in Figure 3a. Contrarily to the Ba and F atoms that have an isotropic ELF around them, the Sn atoms display a large lobe oriented towards the Sn-Sn layer, so that the latter is better described as a Sn-LP-Sn layer. However, such a picture could be misleading as it was obtained for a structure at 0 K. As was shown in previous works, at higher temperatures LP may rotate to accompany the motion of mobile species.^{12,22} We have therefore calculated its orientation along the 900 K trajectory by sampling the maximally localized Wannier functions every 100 fs. The corresponding dipoles remain highly oriented

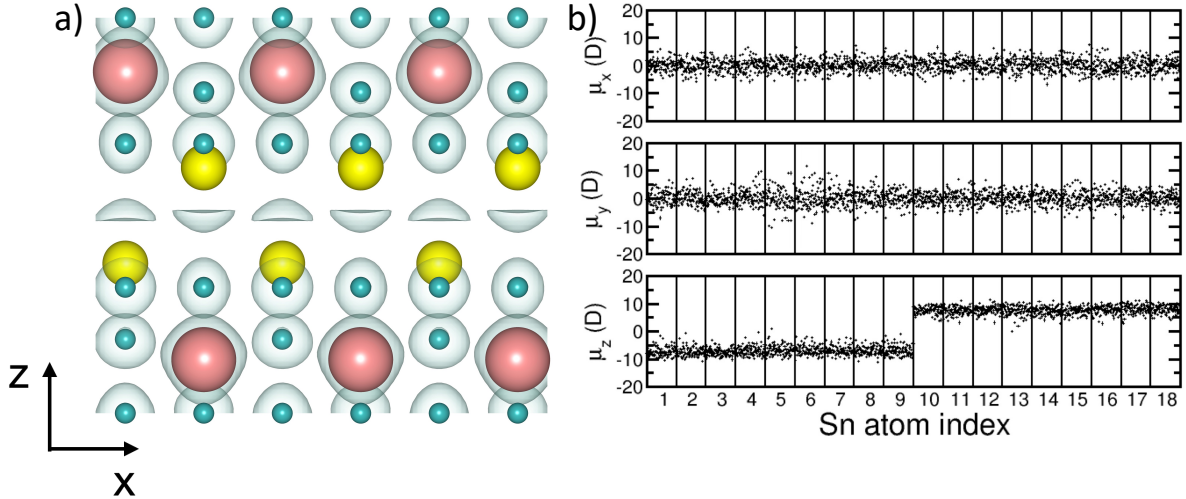


Figure 3: a) Electron localization function calculated for the optimized geometry of tetragonal BaSnF_4 at 0 K. The isosurface level is 0.7. b) Individual dipole components along the three axis for each Sn atom during the ML-MD trajectory at 900 K. Sn atoms with index 1 to 9 are located in the top layer (dipole pointing towards negative z value) while atoms with index 10 to 18 are located in the bottom layer.

as shown in Figure 3b. In particular, from the dipole orientation along the z direction, it is clear that these lone pairs remain directed towards the neighboring layer throughout the simulation, while there is no stereoactivity along the x and y directions. This observation is confirmed by the calculation of the dipole auto-correlation function (see the Supplementary Figure S5). After a quick decay over a timescale lower than 1 ps, which is due to small-amplitude rotations and Sn atom vibrations, the function decays to a very high value with respect to its initial one. We can therefore conclude that contrarily to previous works, the rotational motion of the lone pairs is less significant and do not directly participate in the F^- ions movements. Therefore, in the following subsections, we will detail F^- ion motion and then articulate how the LPs impact the overall conduction indirectly.

Ionic conductivity

The ionic conductivity (σ) of a system can be computed using

$$\sigma = \frac{\beta e^2}{V} \lim_{t \rightarrow \infty} \frac{1}{6t} \langle \left| \sum_i q_i \delta \mathbf{r}_i(t) \right|^2 \rangle \quad (3)$$

where $\delta \mathbf{r}_i(t)$ is the displacement of ion i , which carries a formal charge q_i , in time t , e is the electronic charge, V the volume of the simulation cell, and $\beta = 1/k_B T$ with k_B being the Boltzmann's constant. Note that the sum inside the brackets ensures that all the ionic correlations are taken into account, unlike when using the Nernst-Einstein approximation.

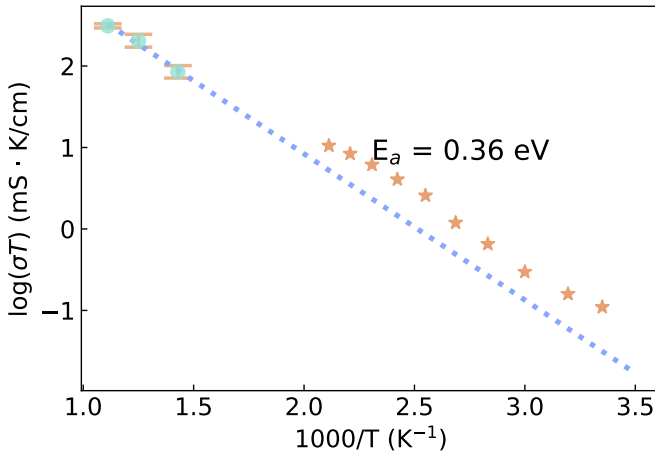


Figure 4: The calculated high-temperature (cyan, circle) and experimental ionic conductivities (orange, star). The experimental data points are collected from ref. ⁵ The fitted linear relationship is extrapolated to low temperature regime to compare with experimental results. The estimated activation energy is 0.36 eV.

Figure 4 shows the computed σT products in the temperature range [700 K, 900 K] together with the experimental ones, which were measured between 298 and 473 K. ⁵ Unfortunately it is not possible to determine the conductivity at lower temperatures from ML-MD simulations since it would require trajectories longer by one or two orders of magnitude to observe the linear régime necessary to use equation 3. The data is represented versus the inverse of temperature, which allows to fit it using the Arrhenius relationship. We obtain an activation energy of 0.36 eV, which is in very good agreement with the experimental value of

0.34 eV.^{5,10} The room temperature ionic conductivity is extrapolated to be $1.0 \times 10^{-4} \text{ S cm}^{-1}$, which is also close to the experimental value of $3.5 \times 10^{-4} \text{ S cm}^{-1}$.^{5,11,38}

An anisotropic diffusion mechanism

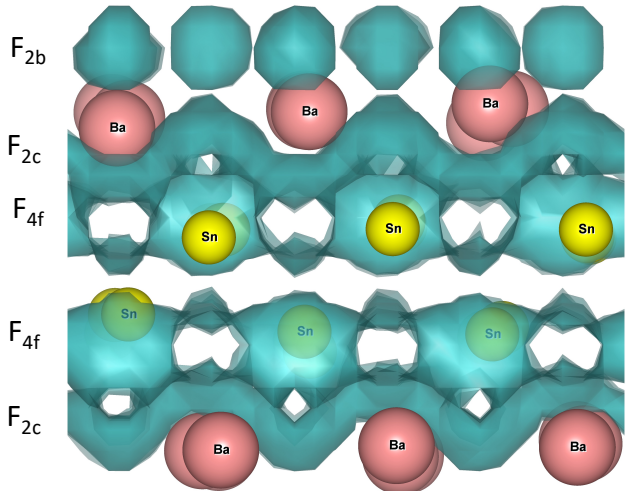


Figure 5: Probability density distribution plots of F^- ions shown in light cyan shades. Labels on the left indicate the Wyckoff positions of different types of F^- ions.

A former NMR study concluded that the diffusion mechanism in tetragonal BaSnF_4 was highly anisotropic, with the largest diffusivity within the Ba-Sn layer.²¹ In our simulation, this anisotropy can clearly be seen by calculating the mean-squared displacements of the fluoride anions along the three cell directions (Supplementary Figure S6). In Supplementary Table 1, we provide the corresponding diffusion coefficients, which quantitatively indicate identical motion along the X and Y direction and a much smaller one along the Z direction to contribute to the 3D diffusivity. This anisotropy is also apparent from the visualization of the probability density of F^- ions as shown in Figure 5: The F^- ions within the Ba-F-Ba layer (F_{2b}) are almost immobile, which is characterized by the spherical disjointed probability densities, while the F^- ions within Ba-F-Sn layers (F_{2c} and F_{4f}) adopt a much more disordered structure, forming an interconnected 2D diffusing network within the layer. Based on this plot, no connections are evident between the sites along the Z axis, both within the Sn-LP-Sn and Ba-F-Ba layers. However, this is a shortcoming of the visualization, since

we observe frequent jumps across the Sn-LP-Sn layer as well as a few ones within the Ba-F-Ba layer during our trajectory. These two conduction pathways will therefore be discussed more thoroughly in the next subsection.

Diffusion along the c-axis

The free energy changes for the fluoride ion jumps along the z direction $F(z)$ of the crystalline structure can be obtained from the probabilities to observe a given position along this direction ($\mathcal{P}(z)$) for all the ions:

$$F(z) = -k_B T \ln \mathcal{P}(z) \tag{4}$$

This function is shown on Figure 6a. The z values are normalized by the crystal cell parameter c , so that $z/c = -0.5$ or $+0.5$ for the F_{2b} sites, -0.35 or $+0.35$ for the F_{2c} sites and -0.18 or $+0.18$ for the F_{4f} sites – the Ba and Sn planes positions are shown as vertical lines to enable a better visualization. We first discuss fluoride ions jumps across the Ba-F-Ba layer, for which a representative event is shown in Figure 6b. Due to the high stability of the F_{2b} , we do not observe the formation of vacancy in this layer during the trajectories. On the contrary, the jump event occurs through the arrival of a fluoride ion coming from the Ba-F-Sn layer, shown in navy blue in the figure. It pushes one of the anions originally present (shown in cyan color), that immediately escapes to the other layer. Following the free energy profile, the energy barrier to consider is therefore the one corresponding to the first event, i.e. the F_{2b} to F_{2c} jump, which is approximately 0.62 eV. Such a large value implies that these events are very rare even at high temperature, and should barely be observed under ambient conditions. The Ba-F-Ba layers hence play the role of barriers that hinder a three-dimensional diffusion in $BaSnF_4$.

The situation is very different concerning the Sn-LP-Sn layer. Indeed, we observe much more frequent jumps during the simulations, and these only imply one anion during each

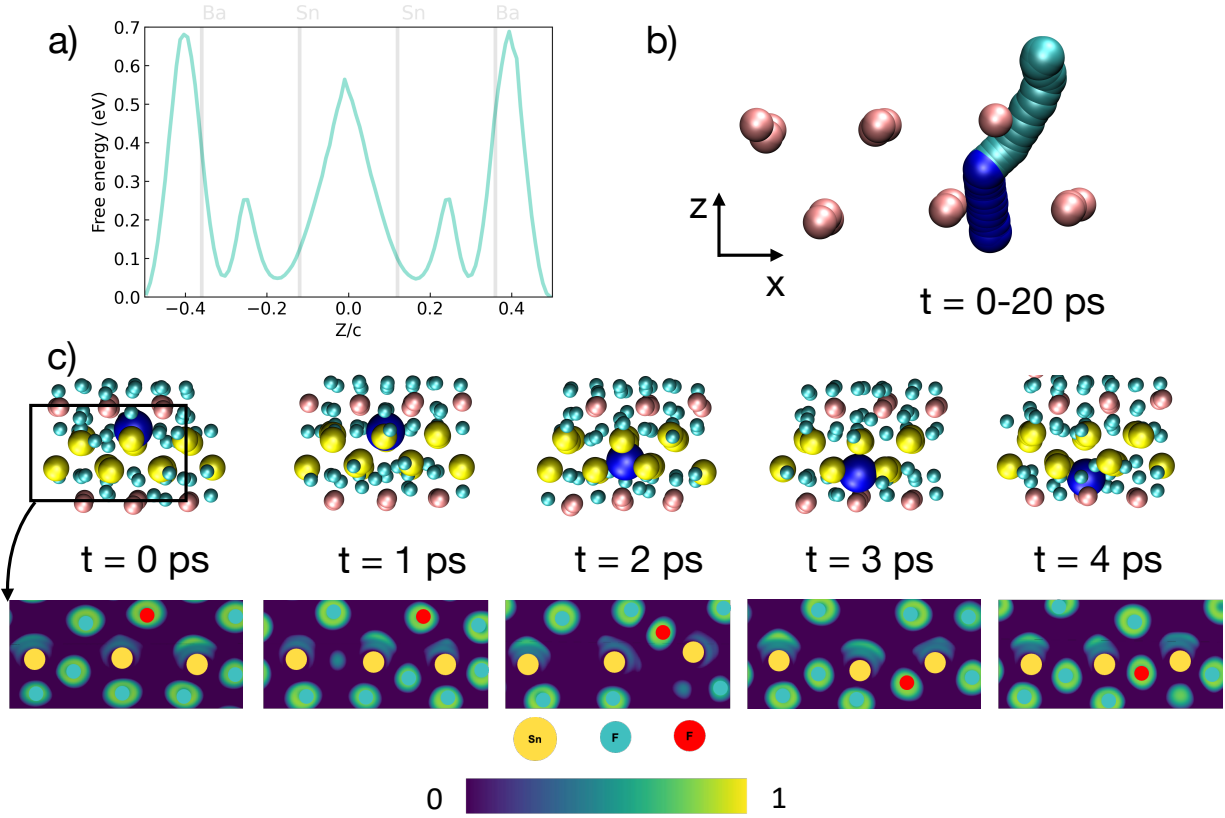


Figure 6: a) Free energy for the fluoride ion motion along c axis. The Ba and Sn layer positions are plotted as light gray vertical lines. Note here the Ba and Sn layer positions are taken from the original relaxed structure and might slightly deviate from their positions during MD simulation. b) Short trajectory showing how F^- ions move across the Ba-F-Ba layer. A first F^- ion from the Ba-F-Sn layer (navy blue) jumps to the Ba-F-Ba layer and pushes the original F^- ion away (cyan). The total timescale of the event is approximately 20 ps. c) Consecutive snapshots where one F^- ion crosses the Sn-LP-Sn layer. The F^- ion is highlighted in blue while the rest of atoms are colored in the same scheme as in Figure 1. At the beginning, it occupies the Ba-F-Sn layer above the Sn-LP-Sn layer. At $t = 2$ ps, it lies within the Sn-LP-Sn layer. It stays less than 1 ps before jumping to the neighboring Ba-F-Sn layer at $t = 3$ ps. Below is shown a projection of the ELF on the plane of the Sn layer for the zone in the black rectangle. The jumping F^- anion is then shown in red for a better visualization.

event. The jumps occur very quickly, with the anion staying only around 1 ps inside the layer due to the absence of stable position, as shown for a typical example on Figure 6c. The free energy barrier associated to these jumps is estimated to be 0.48 eV based on the free energy profile. We do not observe any lateral diffusion within this layer as was hypothesized in the previous NMR study. This is due to the electrostatic repulsion by the electron LPs. The mechanism is therefore different from the *c*-BaSnF₄ phase where the F⁻ ions exchange positions with LPs during their diffusion pathway. As can be seen from the bottom part of Figure 6c, here the LPs of the adjacent atoms are more delocalized when the fluoride anion lies within the Sn-LP-Sn layer, but they quickly recover their initial shape after the jump. This behavior is similar to the selective LPs stereochemical activity in Pb 6s² in previous works.^{16,39} At the transition state, the electron delocalization allows temporary residence of F⁻ ions in the Sn-LP-Sn layer, but there is no electronic paddle-wheel mechanism as was reported for other systems.²²

Influences of Sn²⁺ displacements on F⁻ mobility

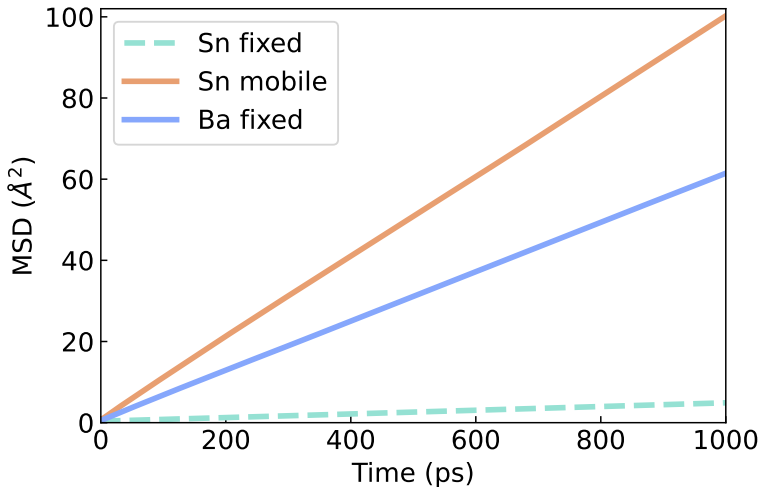


Figure 7: Mean square displacements of mobile F⁻ ions in BaSnF₄ vs time. The results are compared to additional cases in which the Sn (cyan, dashed) and Ba (blue, solid) atoms were held fixed.

The experimental PDF data we presented in Figure 2 highlighted the importance of Sn²⁺

ions disorder. In Figure 6, when F^- ions cross the Sn-LP-Sn layer, it is evident that these Sn^{2+} ions displace from their original positions within a short time. This raises the question of whether the Sn^{2+} influence the F^- ions dynamics and, if yes, of how they modulate the F^- ions mobility. Previous work by Mercadier et al.¹² has shown that Sn LPs orientational dynamics is coupled to F^- dynamics in *c*-BaSnF₄, but compositional disorder of Sn/Ba and relatively low F^- ions mobility make it difficult to investigate the Sn^{2+} positional impacts. On the other hand, in the ordered tetragonal phase, it is convenient to see whether it is the positional shifts or the orientational motion that controls the F^- ion dynamics by performing molecular dynamics under two different situations: when Sn^{2+} ions are mobile and fixed (noted as Sn mobile and Sn fixed in the following context). An additional simulation with fixed Ba^{2+} ions was also performed for comparison purposes.

The MSD of F^- ions in Figure 7 (and also in Supplementary Figure 6) shows a noticeable decrease upon fixing Sn^{2+} ions motion. The diffusivity of Sn mobile case is almost 20 times higher than the one when Sn^{2+} ions are fixed. Such huge differences cannot be ascribed to statistical variances and highlight the important role Sn^{2+} positions play in the BaSnF₄ ionic conduction. On the contrary, the effect of Ba^{2+} ions is marginal, since the diffusivity is only decreased by a factor of roughly 2 when they are fixed in the simulation.

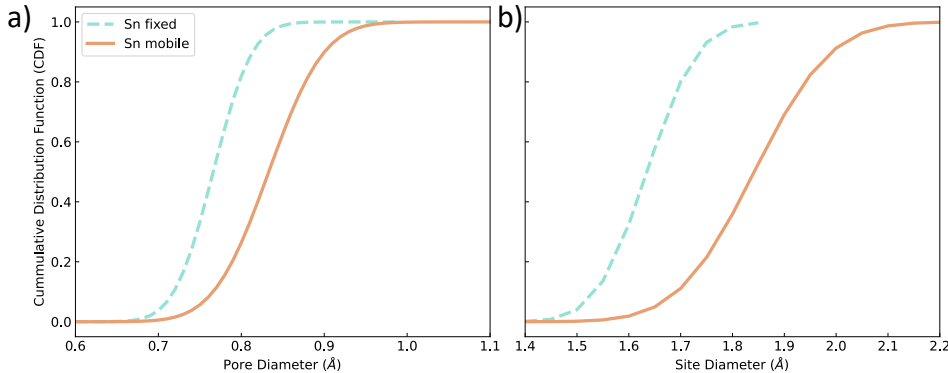


Figure 8: Cumulative distribution function (CDF) of a) Diffusion channel size and b) Size of the largest site. The dashed cyan and solid orange lines represent the distribution obtained for the simulations in which the Sn atoms are respectively fixed and mobile.

Besides the significant changes in MSD, we also note that when Sn^{2+} is mobile, the F^-

ions density in the Ba-F-Sn layer is continuous compared to the apparent disconnection between the F_{4f} and F_{2c} sites when Sn^{2+} is fixed (Supplementary Figure 7). This implies that energy barrier between these two sites is lower when Sn^{2+} is mobile. Instead of forming a rigid network, the latter thus participate actively in the diffusion process. To further understand the effect of Sn^{2+} displacements on F^- ions, we performed topological analysis as shown in Figure 8. The diffusion channel size and free sphere size were computed using the Zeo++ code, which is based on Voronoi decomposition and widely used in porous materials such as MOF.^{40–42} The Voronoi decomposition divides the space into polyhedrons centering the ions in the structure skeleton. The vertices of the polyhedrons, named Voronoi nodes, correspond to the local void space occupiable by a sphere with a radius r . In this study, snapshots were chosen along the trajectory at intervals of 1 ps, and both F_{4f} and F_{2c} ions were selectively removed. Our analysis shows that when Sn^{2+} ions are mobile, both the diffusion channel size and size of the largest sites have increased considerably. The enlarged F^- sites promotes the F^- disordering within the Ba-F-Sn layer, leading to a flattened 2D energy landscape within the plane. Furthermore, The enlarged diffusion channel will allow facile F^- ions transport between neighboring sites, thus creating a disordered layer and boosting the dynamics. Based on our structural analysis, we can conclude that the stereoactivity of the LPs, that do not reorient significantly during the simulations, is at the origin of the high flexibility of the Sn^{2+} atoms. Contrarily to the F anions layer that prevents the Ba^{2+} to be pushed forward to allow diffusion of the mobile fluorides in the Ba-F-Sn layers, there is no short-range repulsion between the LPs and the Sn atoms, so that the latter can more easily arrange their environment to facilitate this diffusion.

Conclusion

In this work, we have simulated the structure and dynamics of the fluoride-ion conductor BaSnF_4 using a ML model. The model keeps the accuracy of the parent DFT calculations,

which is impossible to obtain from conventional classical force fields due to the presence of LPs. It accounts for the Sn atoms displacements with respect to the model structure derived from XRD, allowing for a better refinement of the PDF obtained from high energy X-ray. It also yields an electrical conductivity compatible with experimental measurements, albeit it is not possible to do long enough simulations at low temperatures due to the computational costs. The material is characterized by its layered structure, which gives rise to the presence of an ordered layer of stereoactive LPs pointing within the Sn atoms layers.

The simulations provide a full picture of the fluoride ion diffusion mechanism and its 2D character. The diffusivity is much larger along the X and Y axis since it occurs mostly within the Ba-F-Sn layers. However, the LPs play an important role. Due to the fact that they do not display a strong repulsion at short range as ions would do, they allow the F^- ions to jump across the Sn-LP-Sn layer, leaving vacancies behind them. Neighboring F^- ions will quickly migrate to these vacant sites, forming a percolation network. Considering the large number of F^- ions that jump back and forth between neighboring Ba-F-Sn layers, many vacancies emerge and vanish simultaneously.

Besides the diffusion within the Sn-LP-Sn layer, we also clarified the exchange of F^- ions between Ba-F-Sn and Ba-F-Ba layer. This process differs from the previous one in that it involves a pair of anions instead of one. The F^- from the Ba-F-Sn layer enters the Ba-F-Ba layer and simultaneously pushes the original F^- to the next layer. Contrarily to the previous diffusion pathway, in that case the F^- ion must then overcome a much higher migration energy, so such jumps are very rare events of the simulations even at high temperature.

Finally, the important role of Sn^{2+} translational motion was highlighted. We showed that fixing the Sn^{2+} movements decreases the diffusion channel size and the size of the largest sites, thereby freezing out the F^- ion dynamics. The flexibility of Sn^{2+} ions originates from the presence of the LPs, which, unlike the F^- ions in the Ba-F-Ba layer, only interact with the other species through Coulombic interactions. Their extension adapts temporarily to allow for the Sn atoms to penetrate within the layer, thus extending the volume available

locally within the Ba-F-Sn layer for the fluoride ions to diffuse.

Acknowledgments

Part of this work was supported by a French government grant managed by the Agence Nationale de la Recherche under the France 2030 program, reference 23-PEBA-0002. DD wished to thank Olaf Borkiewicz for providing the PDF data. This research used resources of the Advanced Photon Source, a US Department of Energy (DOE) Office of Science User Facility operated for the DOE Office of Science by Argonne National Laboratory under Contract No. DE-AC02-06CH11357.

References

- (1) Xiao, A. W.; Galatolo, G.; Pasta, M. The Case for Fluoride-Ion Batteries. *Joule* **2021**, *5*, 2823–2844.
- (2) Nowroozi, M. A.; Mohammad, I.; Molaiyan, P.; Wissel, K.; Munnangi, A. R.; Clemens, O. Fluoride Ion Batteries – Past, Present, and Future. *J. Mater. Chem. A* **2021**, *9*, 5980–6012.
- (3) Anji Reddy, M.; Fichtner, M. Batteries Based on Fluoride Shuttle. *J. Mater. Chem.* **2011**, *21*, 17059.
- (4) Chaudhuri, S.; Wang, F.; Grey, Clare P. Resolving the Different Dynamics of the Fluorine Sublattices in the Anionic Conductor BaSnF₄ by Using High-Resolution MAS NMR Techniques. *J. Am. Chem. Soc.* **2002**, *124*, 11746–11757.
- (5) Mohammad, I.; Witter, R.; Fichtner, M.; Anji Reddy, M. Room-Temperature, Rechargeable Solid-State Fluoride-Ion Batteries. *ACS Appl. Energy Mater.* **2018**, *1*, 4766–4775.

- (6) Mohammad, I.; Witter, R.; Fichtner, M.; Reddy, M. A. Introducing Interlayer Electrolytes: Toward Room-Temperature High-Potential Solid-State Rechargeable Fluoride Ion Batteries. *ACS Appl. Energy Mater.* **2019**, *2*, 1553–1562.
- (7) Chen, H.; Aalto, T.; Vanita, V.; Clemens, O. Effect of Uniaxial Stack Pressure on the Performance of Nanocrystalline Electrolytes and Electrode Composites for All-Solid-State Fluoride-Ion Batteries. *Small Struct.* **2024**, *5*, 2300570.
- (8) Xiong, L.; Wen, P.; Zhang, Y.; Liu, X.; Ning, J.; Wang, X.; Wang, H.; Yang, Z. Exploring Efficient Solid Electrolyte Based on Nd Doped BaSnF₄ for Fluoride-Ion Batteries at Atomic Scale. *J. Power Sources* **2022**, *518*, 230718.
- (9) Zang, Z.; Liu, J.; Tao, X.; Zou, C.; Chen, X.; Yi, L.; Chang, B.; Wang, X. Mn²⁺ Doped BaSnF₄ -Based Solid State Electrolyte for Room-Temperature Fluoride Ion Batteries. *J. Electroanal. Chem.* **2023**, *930*, 117145.
- (10) Dénès, G.; Birchall, T.; Sayer, M.; Bell, M. F. BaSnF₄ — A New Fluoride Ionic Conductor with the α -PbSnF₄ Structure. *Solid State Ion.* **1984**, *13*, 213–219.
- (11) Ahmad, M. M.; Yamane, Y.; Yamada, K. Structure, Ionic Conduction, and Giant Dielectric Properties of Mechanochemically Synthesized BaSnF₄. *J. Appl. Phys.* **2009**, *106*, 074106.
- (12) Mercadier, B.; Coles, S. W.; Duttine, M.; Legein, C.; Body, M.; Borkiewicz, O. J.; Lebedev, O.; Morgan, B. J.; Masquelier, C.; Dambournet, D. Dynamic Lone Pairs and Fluoride-Ion Disorder in Cubic-BaSnF₄. *J. Am. Chem. Soc.* **2023**, *145*, 23739–23754.
- (13) Denes, G.; Yu, Y. H.; Tyliczszak, T.; Hitchcock, A. P. Sn-K, Pb-L₃, and Ba-L₃ EXAFS, X-ray Diffraction and ¹¹⁹Sn Mössbauer Spectroscopic Studies of Ordered M₂SnF₄ (M = Pb and Ba) Fluoride Ionic Conductors with the α -PbSnF₄ Structure. *J. Solid State Chem.* **1991**, *91*, 1–15.

- (14) Carnevali, V.; Mukherjee, S.; Voneshen, D. J.; Maji, K.; Guilmeau, E.; Powell, A. V.; Vaqueiro, P.; Fornari, M. Lone Pair Rotation and Bond Heterogeneity Leading to Ultralow Thermal Conductivity in Aikinite. *J. Am. Chem. Soc.* **2023**, *145*, 9313–9325.
- (15) Gomes, E. O.; Gouveia, A. F.; Gracia, L.; Lobato, Á.; Recio, J. M.; Andrés, J. A. Chemical-Pressure-Induced Phase Transition Controlled by Lone Electron Pair Activity. *J. Phys. Chem. Lett.* **2022**, *13*, 9883–9888.
- (16) Matsui, N.; Murakami, M.; Mori, K.; Saito, T.; Shimizu, K.; Suzuki, K.; Kanno, R. Effect of Pb 6s² Lone Pair on the Potential Flattening of Fluoride-Ion Conduction in Perovskite-Type Fluoride. *J. Mater. Chem. A* **2024**, *12*, 3989–3996.
- (17) Walsh, A.; Payne, D. J.; Egdell, R. G.; Watson, G. W. Stereochemistry of Post-Transition Metal Oxides: Revision of the Classical Lone Pair Model. *Chem. Soc. Rev.* **2011**, *40*, 4455–4463.
- (18) Kannan, C. V.; Shimamura, K.; Zeng, H. R.; Kimura, H.; Villora, E. G.; Kitamura, K. Ferroelectric and Anisotropic Electrical Properties of BaMgF₄ Single Crystal for Vacuum UV Devices. *J. Appl. Phys.* **2008**, *104*, 114113.
- (19) Waghmare, U. V.; Spaldin, N. A.; Kandpal, H. C.; Seshadri, R. First-Principles Indicators of Metallicity and Cation off-Centricity in the IV-VI Rocksalt Chalcogenides of Divalent Ge, Sn, and Pb. *Phys. Rev. B* **2003**, *67*, 125111.
- (20) Castiglione, M.; Madden, P. A.; Berastegui, P.; Hull, S. The Crystal Structure of α -PbSnF₄ and Its Anion Diffusion Mechanism. *J. Phys. Condens. Matter* **2005**, *17*, 845.
- (21) Chaudhuri, S.; Castiglione, M.; Wang, F.; Wilson, M.; Madden, P. A.; Grey, C. P. Study of Fluoride Ion Motions in PbSnF₄ and BaSnF₄ Compounds With Molecular Dynamics Simulation and Solid State NMR Techniques. *MRS Proc.* **2000**, *658*, GG10.9.

- (22) Dhattarwal, H. S.; Somni, R.; Remsing, R. C. Electronic Paddle-Wheels in a Solid-State Electrolyte. *Nat. Commun.* **2024**, *15*, 121.
- (23) Kresse, G.; Furthmüller, J. Efficient Iterative Schemes for Ab Initio Total-Energy Calculations Using a Plane-Wave Basis Set. *Phys. Rev. B* **1996**, *54*, 11169–11169.
- (24) Kresse, G.; Joubert, D. From Ultrasoft Pseudopotentials to the Projector Augmented-Wave Method. *Phys. Rev. B* **1999**, *59*, 1758–1758.
- (25) Lian, X.; Salanne, M. Capturing the Interactions in the BaSnF₄ Ionic Conductor: Comparison between a Machine-Learning Potential and a Polarizable Force Field. *J. Chem. Phys.* **2023**, *159*, 144705.
- (26) Jinnouchi, R.; Karsai, F.; Verdi, C.; Asahi, R.; Kresse, G. Descriptors Representing Two-and Three-Body Atomic Distributions and Their Effects on the Accuracy of Machine-Learned Inter-Atomic Potentials. *J. Chem. Phys.* **2020**, *152*, 234102.
- (27) Jinnouchi, R.; Karsai, F.; Kresse, G. On-the-Fly Machine Learning Force Field Generation: Application to Melting Points. *Phys. Rev. B* **2019**, *100*, 014105.
- (28) Jinnouchi, R.; Lahnsteiner, J.; Karsai, F.; Kresse, G.; Bokdam, M. Phase Transitions of Hybrid Perovskites Simulated by Machine-Learning Force Fields Trained on the Fly with Bayesian Inference. *Phys. Rev. Lett.* **2019**, *122*, 225701.
- (29) Pizzi, G. *et al.* Wannier90 as a Community Code: New Features and Applications. *J. Phys. Condens. Matter* **2020**, *32*, 165902.
- (30) Aguado, A.; Bernasconi, L.; Jahn, S.; Madden, P. A. Multipoles and Interaction Potentials in Ionic Materials from Planewave-DFT Calculations. *Faraday Discuss.* **2003**, *124*, 171–184.
- (31) Wang, V.; Xu, N.; Liu, J.-C.; Tang, G.; Geng, W.-T. VASPKIT: A User-Friendly

- Interface Facilitating High-Throughput Computing and Analysis Using VASP Code. *Comput. Phys. Commun.* **2021**, *267*, 108033.
- (32) Ong, S. P.; Richards, W. D.; Jain, A.; Hautier, G.; Kocher, M.; Cholia, S.; Gunter, D.; Chevrier, V. L.; Persson, K. A.; Ceder, G. Python Materials Genomics (Pymatgen): A Robust, Open-Source Python Library for Materials Analysis. *Comput. Mater. Sci.* **2013**, *68*, 314–319.
- (33) Michaud-Agrawal, N.; Denning, E. J.; Woolf, T. B.; Beckstein, O. MDAnalysis: A Toolkit for the Analysis of Molecular Dynamics Simulations. *J. Comput. Chem.* **2011**, *32*, 2319–2327.
- (34) Gowers, R. J.; Linke, M.; Barnoud, J.; Reddy, T. J. E.; Melo, M. N.; Seyler, S. L.; Domański, J.; Dotson, D. L.; Buchoux, S.; Kenney, I. M.; Beckstein, O. MDAnalysis: A Python Package for the Rapid Analysis of Molecular Dynamics Simulations. *Proc. 15th Python Sci. Conf.* **2016**, 98–105.
- (35) Qiu, X.; Thompson, J. W.; Billinge, S. J. L. PDFgetX2: A GUI-driven Program to Obtain the Pair Distribution Function from X-ray Powder Diffraction Data. *J. Appl. Crystallogr.* **2004**, *37*, 678–678.
- (36) Farrow, C. L.; Juhas, P.; Liu, J. W.; Bryndin, D.; Božin, E. S.; Bloch, J.; Proffen, T.; Billinge, S. J. L. PDFfit2 and PDFgui: Computer Programs for Studying Nanostructure in Crystals. *J. Phys. Condens. Matter* **2007**, *19*, 335219.
- (37) Silvi, B.; Savin, A. Classification of Chemical Bonds Based on Topological Analysis of Electron Localization Functions. *Nature* **1994**, *371*, 683–686.
- (38) Preishuber-Pflügl, F.; Epp, V.; Nakhal, S.; Lerch, M.; Wilkening, M. Defect-enhanced F⁻ Ion Conductivity in Layer-structured Nanocrystalline BaSnF₄ Prepared by High-energy Ball Milling Combined with Soft Annealing. *Phys. Status Solidi C* **2015**, *12*, 10–14.

- (39) Walsh, A.; Watson, G. W. The Origin of the Stereochemically Active Pb(II) Lone Pair: DFT Calculations on PbO and PbS. *Journal of Solid State Chemistry* **2005**, *178*, 1422–1428.
- (40) Martin, R. L.; Smit, B.; Haranczyk, M. Addressing Challenges of Identifying Geometrically Diverse Sets of Crystalline Porous Materials. *J. Chem. Inf. Model.* **2012**, *52*, 308–318.
- (41) Willems, T. F.; Rycroft, C. H.; Kazi, M.; Meza, J. C.; Haranczyk, M. Algorithms and Tools for High-Throughput Geometry-Based Analysis of Crystalline Porous Materials. *Microporous Mesoporous Mater.* **2012**, *149*, 134–141.
- (42) Martin, R. L.; Haranczyk, M. Construction and Characterization of Structure Models of Crystalline Porous Polymers. *Cryst. Growth Des.* **2014**, *14*, 2431–2440.